Supporting Information

Achieving a safe high-voltage Lithium-metal battery by tailoring electrolyte system

Kai Lan, Jancong Cheng, XinXin Yang, Jingmin Fan, Mingseng Zheng, Ruming Yuan*, Quanfeng Dong*

Methods

Preparation of electrodes and electrolyte

Li foils (1 mm thick, Φ =15.6 mm) was purchased from China Energy Lithium Co.. NCM811 ($LiNi_{0.8}Co_{0.1}Mn_{0.1}O_2$) was purchased from Bidepharma. Ethylene carbonate (EC), fluoroethylene carbonate (FEC), diethyl carbonate (DEC), lithium hexafluorophosphate ($LiPF_6$) and Lithium Difluoro(oxalato)borate (LiDFOB) are purchased from DoDo chem. Trimethyl phosphate (TEP), Trimethyl phosphate (TMP) and Tri(2,2,2-trifluoroethyl) phosphate (TFP) are purchased from Shanghai Aladdin Biochemical Technology Co. Molecular sieve is used to remove traces of water from solvents. The cathode slurry was prepared by mixing 90 wt% NCM811, 5 wt% Super-P, 5 wt% polyvinylidene difluorides (PVDF) into dewatered Nmethyl-2-pyrrolidone (NMP). After coating the slurry on aluminum foil with 13 mm diameter, NCM811 cathode can be obtained after drying at 120°C for 48h under vacuum. Li anode with limited lithium being used in the Li||NCM811 was prepared by depositing a certain amount of Li on a copper foil (15 mm diameter) with a current density of 0.2 mA cm^{-2} using different electrolytes. Electrolytes were prepared and stirring overnight. Electrolyte preparation and cell assembly are performed in an argon glove box (water content and oxygen content are below 0.1 ppm).

Materials characterization

Raman spectroscopic characterization of electrolyte was investigated by Raman

spectroscopy (XploRA) with a scan range of 300-1800 cm^{-1}. FTIR spectra of the electrolytes were collected by a PerkinElmer Frontier instrument. The nuclear magnetic resonance (NMR) spectroscopy of ^{7}Li was collected by 600MHz Nuclear Magnetic Resonance Instrument. Scanning electron microscope (SEM) images were obtained by FE-SEM (HITACHI S-4800) operated at 15 kV. Transmission electron microscope (TEM) images were collected by Talos F200s. X-ray photoelectron spectroscopy (XPS) was investigated by PHI QUAN-TUM 2000 with an Ar^{+} gun. The correction of the binding energy in XPS plots is based on the spectrum of C 1s, and the bond energy of C-C/C-H is set to 284.8 eV.

Electrochemical measurements

All cells used in the electrochemical measurements were assembled with 2023-type coin cells. The Celgard 2400 polypropylene was used the membrane. In the Li||NCM811 cells with excess Li, 1.0 mm Li foil was employed as the counter/reference electrode and NCM811 were employed as the working electrode. The electrochemical performance of cells were performed on Neware BTS 4000. The cyclic scanning voltammetry (CV) curves were collected at CHI 760E electrochemical workstation (ChenHua Co., Ltd., Shanghai). Electrochemical impedance spectroscopy (EIS) is performed on an IM6, Zahner Elektrik pristine in the frequency range 100 kHz to 100 mHz with an AC amplitude of 5 mV. All electrochemical tests are performed at room temperature.

The activation energy for Li^{+} migration through the SEI and the charge transfer process was calculated by Arrhenius equation. The Li||Li symmetric cells with different electrolyte were first performed 10 charge-discharge cycles to form the SEI on the electrode surface. And then, the EIS was tested at different temperature (10-60℃). The charge transfer resistance and charge transfer resistance were obtained by fitting the Nyquist plots using Zview software according to the equivalent circuit. The data was used to plot ln(1/R) vs. 1000/T curves for each process. Subsequently, the activation energy for each process was calculated by Arrhenius equation as follow:

$$\frac{1}{R(SEI,ct)} = Ae^{-Ea/RT}$$

where A is the pre-exponential constant, R is the gas constant, and Ea is the activation energy.

$$Ea = (-19.144 \times slope) kJ\ mol^{-1}$$

Calculation method

AIMD Simulation: Ab initio Molecular Dynamics (AIMD) simulations were performed using the Vienna Ab initio Simulation Package (VASP 5.4) based on the pseudopotential plane-wave approach. The Perdew-Burke-Ernzerhof generalized gradient approximation (GGA-PBE) was utilized to represent the exchange-correlation functional, with a cutoff energy of 400 eV. The initial configurations of LiDFOB, FEC, TEP and TFP were optimized using Gaussian09 program with M06-2X/6-311+G(d,p). The LiDFOB salt/solvent mixtures were prepared by randomly placing the molecules in the simulation box based on their experimental densities and molar ratios. A cubic-shaped simulation box of length 1.538 nm was used for all dimensions. Then AIMD simulations were performed at 300 K using the NVT ensemble with a time step of 1.0 fs. Temperature oscillations were controlled using a Nose thermostat with a Nose-mass parameter of 1.0. A Monkhorst-Pack k-point mesh grid scheme with a 1×1×1 grid was used. The systems were equilibrated for at least 60 ps before the production run of 10 ps. Radial distribution functions were obtained by the Visual Molecular Dynamics (VMD) software. The VESTA program was used to sample the most probable solvation shells from the simulation trajectory.

DFT calculations: DFT calculations in this work were performed using Gaussian 09 program. In present work, the M06-2X functional was adopted, which had been widely used in organic reactions. Geometry optimizations and energy calculations were performed at the M06-2X/6-311+G(d,p) basis set for all atoms. The SMD implicit solvent model was used with the acetone as the implicit solvent.

The [Li^+-solvent/anion] formation energy can be defined as:

$$\Delta E = E[Li^+ - solvent] - E[Li^+] - E[solvent]$$

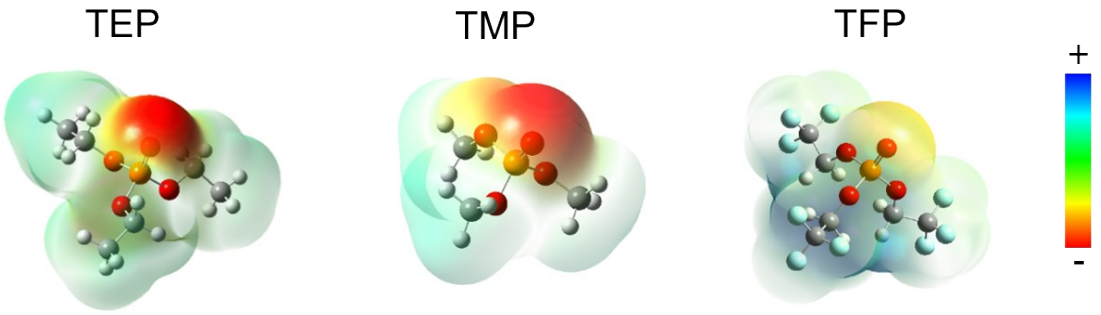

Figure S1. Plot of electrostatic potential distribution of different phosphate esters.

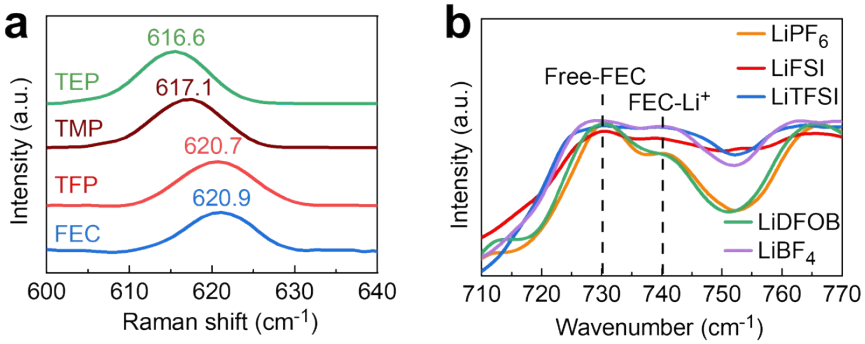

Figure S2. (a) $DFOB^-$ Raman spectra in electrolytes with pure solvent (LiDFOB:solvent=1:10 by mol). (b) FTIR test of FEC in the electrolytes of 1 M lithiun salt in FEC solvent.

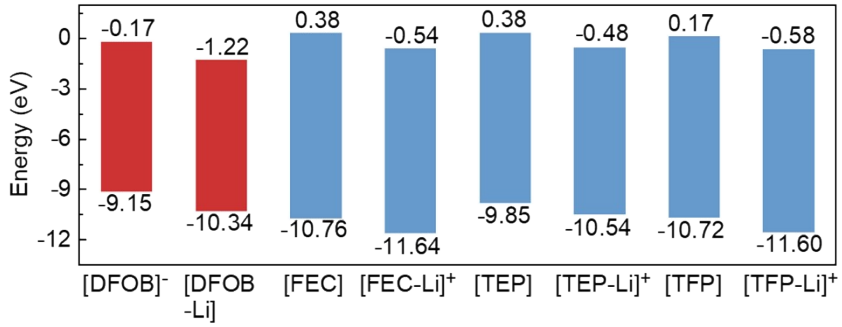

Figure S3. The LUMO and HOMO energy levels of different electrolyte components calculated by DFT.

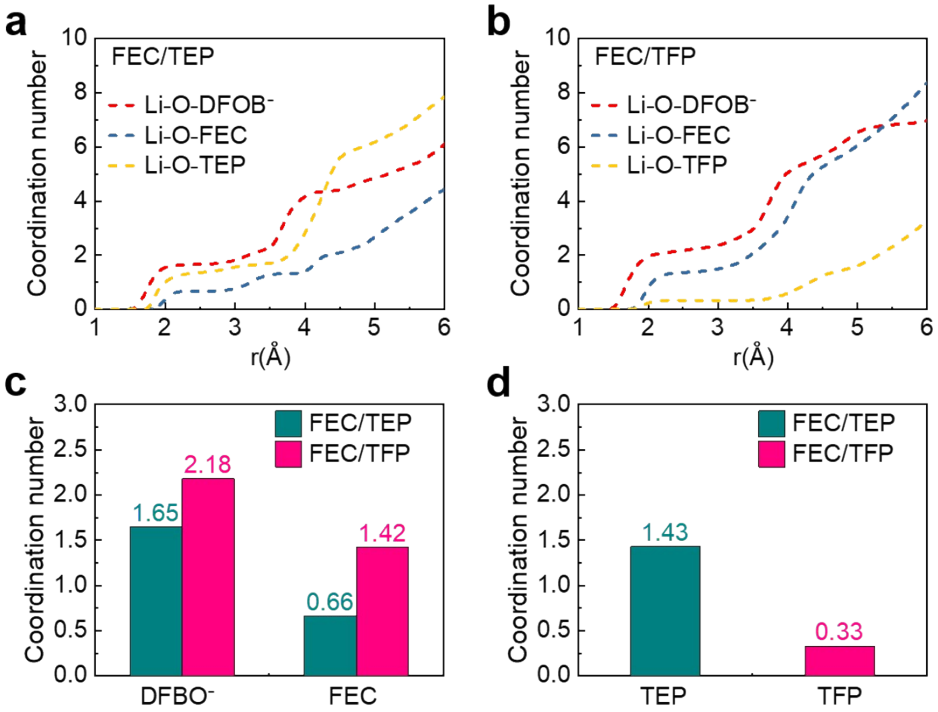

Figure S4. The radial distribution of Li^+ from AIMD simulation in (a) the FEC/TEP electrolyte and (b) the FEC/TFP electrolyte. (c-d) the detail coordination number of electrolyte components located about 2.0-2.5 Å away from the Li^+.

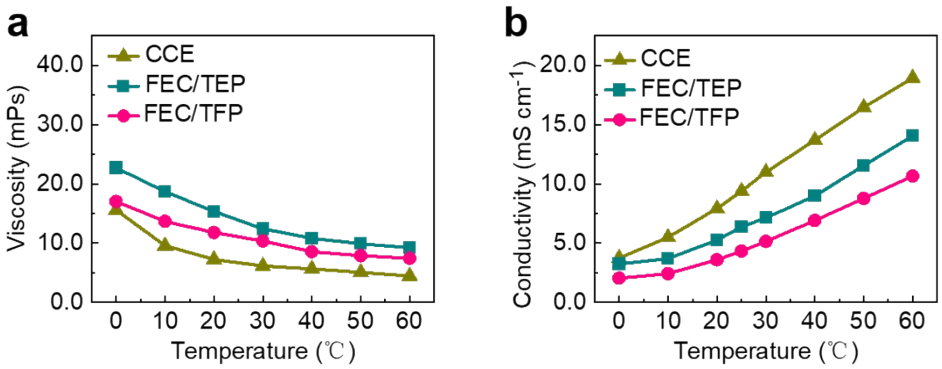

Figure S5. (a) Viscosity and (b) ionic conductivity of the electrolyte at different temperatures.

Table S1. Ionic conductivity of FEC/TFP electrolytes versus recently reported highly concentrated/locializesd highly concentrated electrolytes.

Electrolytes	FEC/TFP	10M LiFSI-DMC	2M LiTFSI + 2M LIDFOB in DME	1.0LiFSI-1.3DMAC-2.0HFE	1.5M LiFSI-1.2DME-3.0TTE
Test temperature (℃)	25	25	30	25	25
Conductivity (mS cm^{-1})	4.4	~1.8	2.31	1.63	2.44
Literatures	This work	1	2	3	4

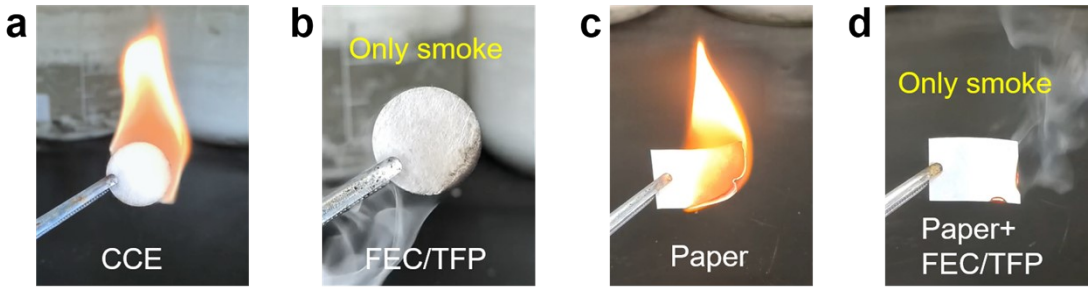

Figure S6. Ignition test and flame retardant test of electrolytes in air.

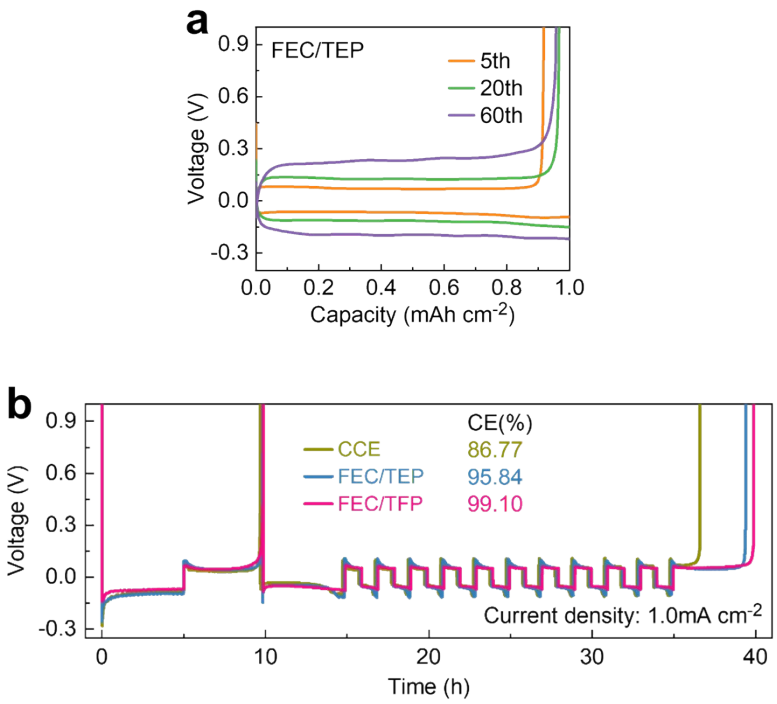

Figure S7. (a) Charge-discharge curves of the FEC/TFP electrolyte under 1 mA cm^{-2} - 1 mAh cm^{-2} test conditions in Li||Cu batteries. (b) Average coulombic efficiency testing of Li deposition-stripping was conducted using the Aurbach test method under a current density of 1 mA cm^{-2}.

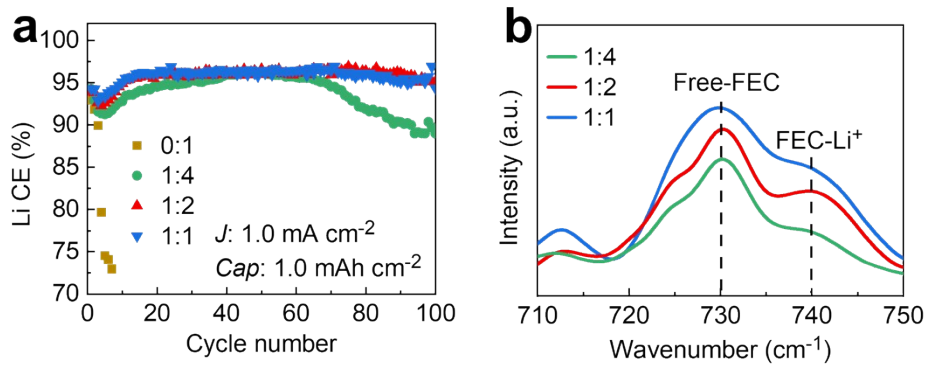

Figure S8. (a) The CE of Li||Cu cells with the electrolytes in which 1.0 M LiDFOB was solvated in the electrolytes with different ratio of FEC:TFP by volum. (b) FTIR spectrum of FEC in the electrolytes.

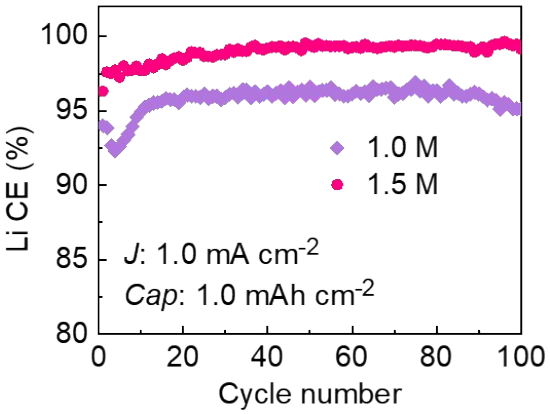

Figure S9. The CE of the FEC/TFP (FEC:TFP=1:2 by vol.) electrolyte in Li||Cu cells with different LiDFOB concentration (1.0 M and 1.5 M) under 1 mA cm^{-2}-1 mAh cm^{-2} test conditions.

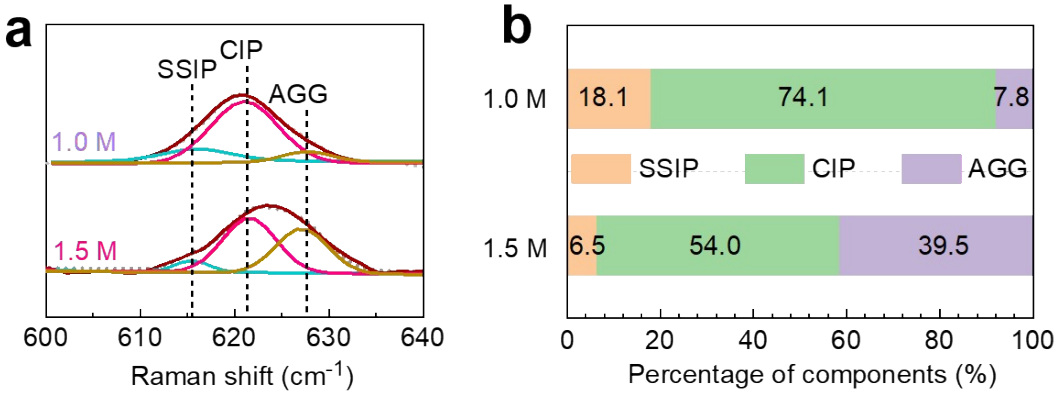

Figure S10. (a) Raman spectra of $DFOB^-$ in the FEC/TFP (FEC:TFP=1:2 by vol.) electrolyte with different LiDFOB concentration (1.0 M and 1.5 M). (b) Corresponding ratios of the amount of anions in different coordination states, obtained by mathematical integration.

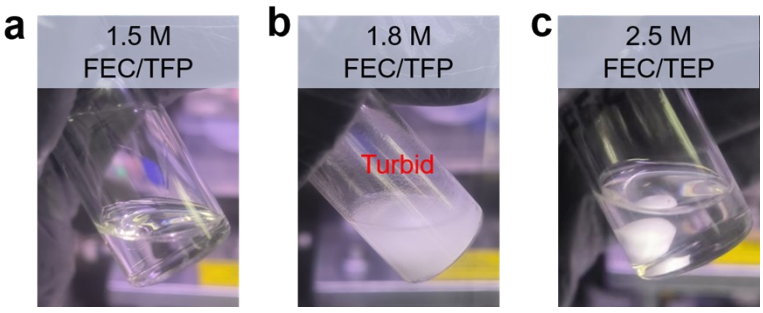

Figure S11. Photographs of LiDFOB solubilization. The FEC/TFP electrolyte (FEC:TFP=1:2 by vol.) with (a) 1.5M and (b) 1.8M. (c) 2.5 M LiDFOB in the FEC/TEP (FEC:TEP=1:2 by vol.) electrolyte.

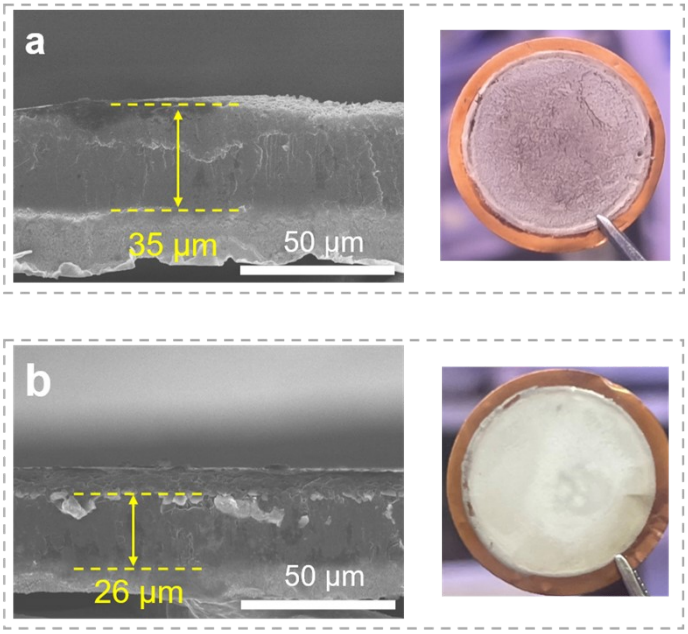

Figure S12. SEM images and digital photographs of Li deposition. Lithium was deposited at a current density of 1 mA cm^{-2} on a copper current collector to achieve a deposition of 5 mAh cm^{-2}, in (a) the FEC/TEP and (b) FEC/TFP electrolytes, respectively.

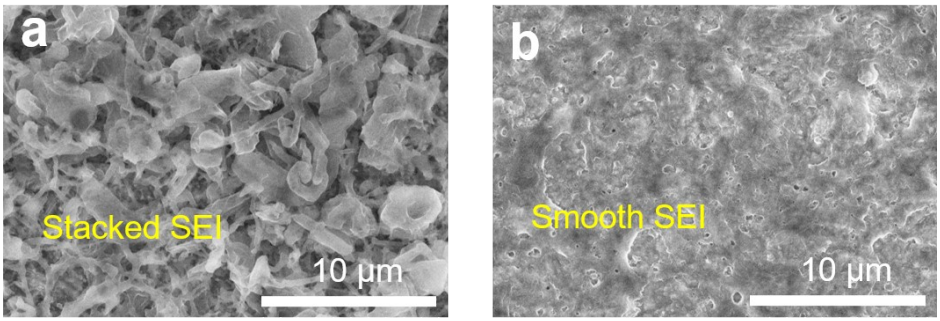

Figure S13. SEM images of Li stripping. Lithium was initially deposited at 5 mAh cm^{-2} on a copper current collector, followed by charging the Li||Cu cell to 1 V to strip the lithium, respectively, in (a) FEC/TEP and (b) FEC/TFP electrolytes.

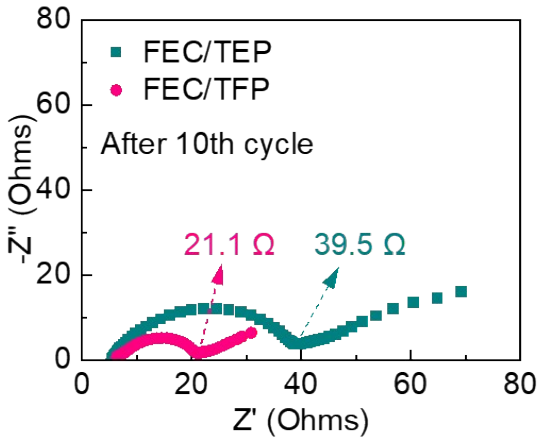

Figure S14. Electrochemical Impedance Spectroscopy (EIS) testing was conducted on Li||Li symmetric cells after 10 cycles at a current density of 1 mA cm^{-2} - 1 mAh cm^{-2}, employing different electrolytes.

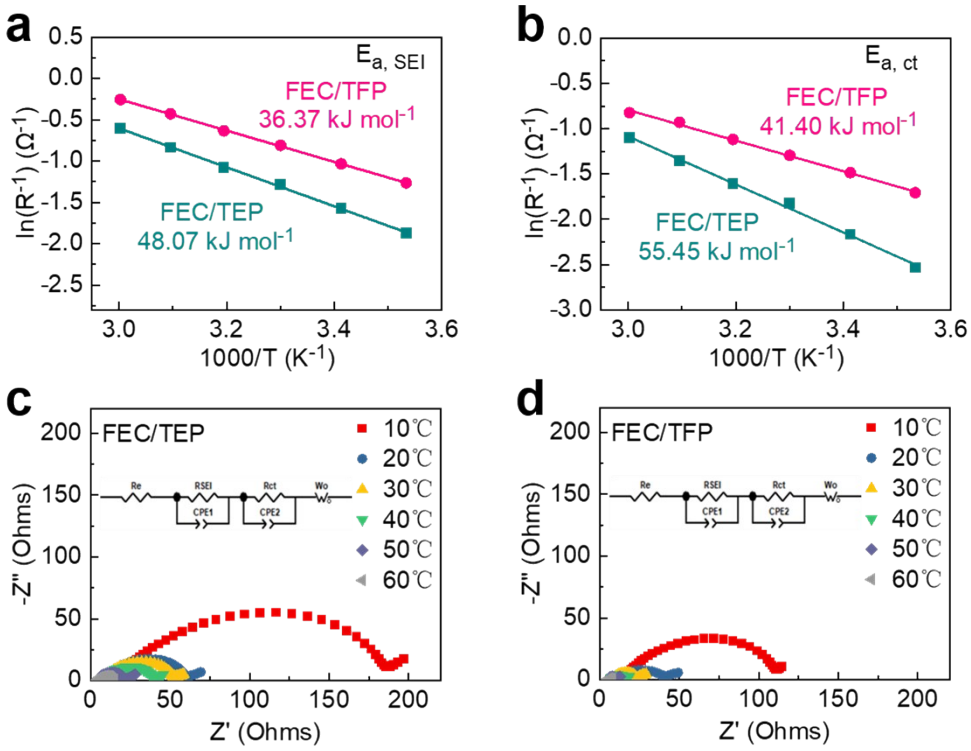

Figure S15. Lithium metal electrode activation energy test. Li||Li symmetric cells with different electrolytes were subjected to EIS tests at different temperatures after 10 cycles at 1 mA cm^{-2} - 1 mAh cm^{-2}. The obtained impedance values are used to calculate $E_{a, SEI}$ and $E_{a, ct}$. (a) Calculated $E_{a, SEI}$. (b) Calculated $E_{a, ct}$. (c) and (d) are the Nyquist plots at different temperatures in the FEC/TEP and FEC/TFP electrolytes, respectively. The insets in (c) and (d) are the corresponding equivalent circuit diagrams.

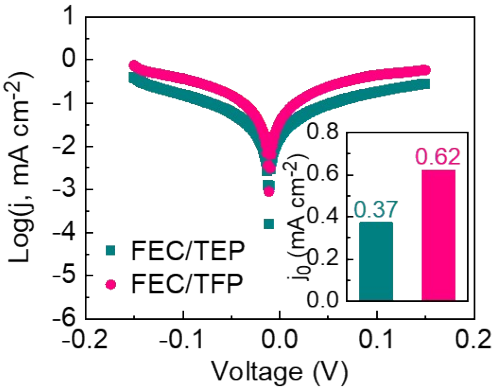

Figure S16. Tafel slope and exchange current density (J_0) tests. Li||Li symmetric cells with different electrolytes were tested after 10 cycles at 1 mA cm^{-2} - 1 mAh cm^{-2}.

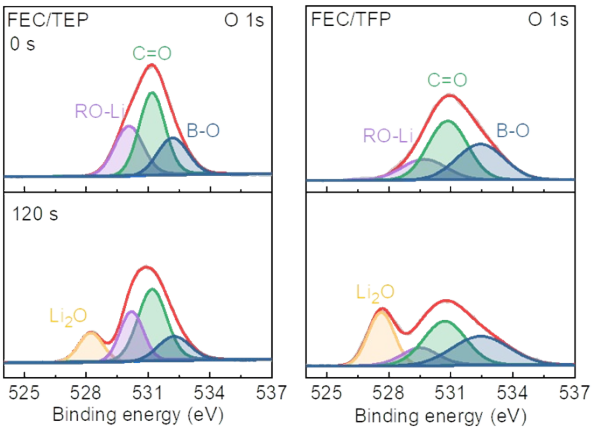

Figure S17. O 1s XPS spectra of lithium metal anode SEI with different sputtering times in different electrolytes. The peaks located at 528.2, 530.2, 531.2and 532.3 belong to Li_2O, B-O, C=O and RO-Li, respectively.[5]

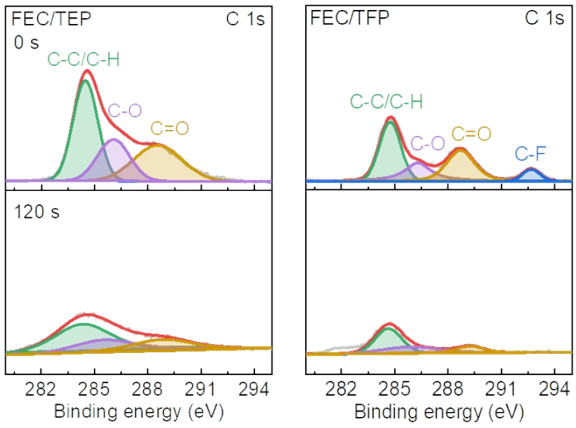

Figure S18. C 1s XPS spectra of lithium metal anode SEI with different sputtering times in different electrolytes. Among them, the peaks located at 284.8, 286.2, 288.7 and 292.7 are belong to C-C/C-H, C-O, C=O and C-F, respectively.[2]

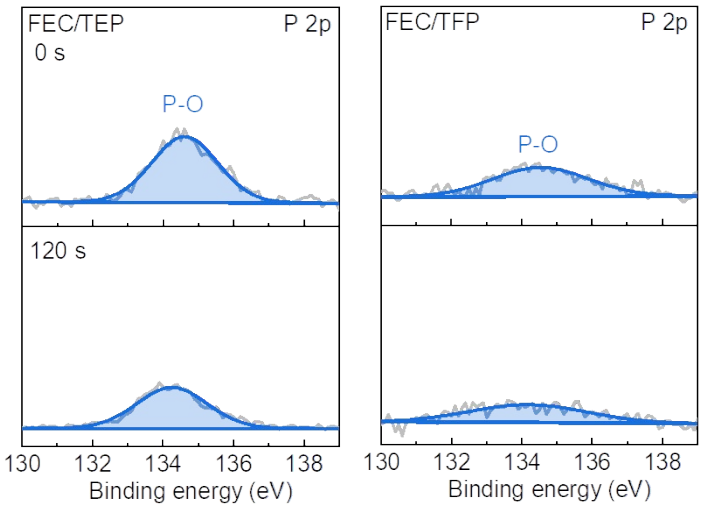

Figure S19. P 2p XPS spectra of lithium metal anode SEI with different sputtering times in different electrolytes. Among them, the peak of the spectrum located at 134.3 belongs to P-O. respectively.[6]

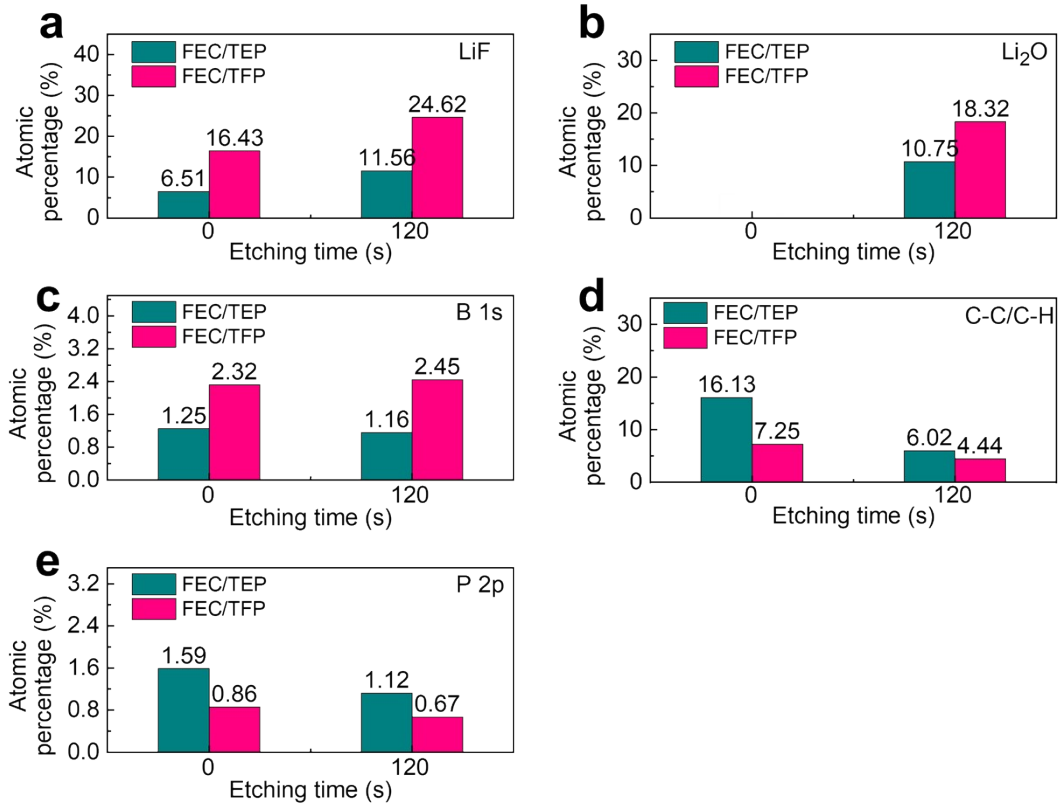

Figure S20. Atomic percentage of SEI component at the lithium metal in different electrolytes for different sputtering times.

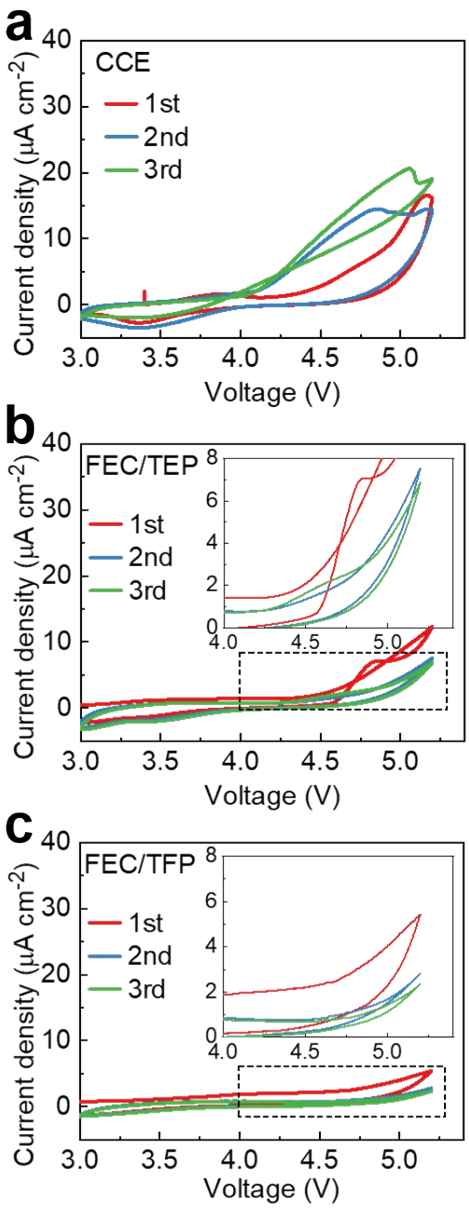

Figure S21. Oxidative stability tests of electrolytes. CV tests were performed in Li||Al cells using (a) CCE, (b) FEC/TEP and (c) FEC/TFP electrolyte, respectively, at a sweep rate of 1 mV s^{-1}.

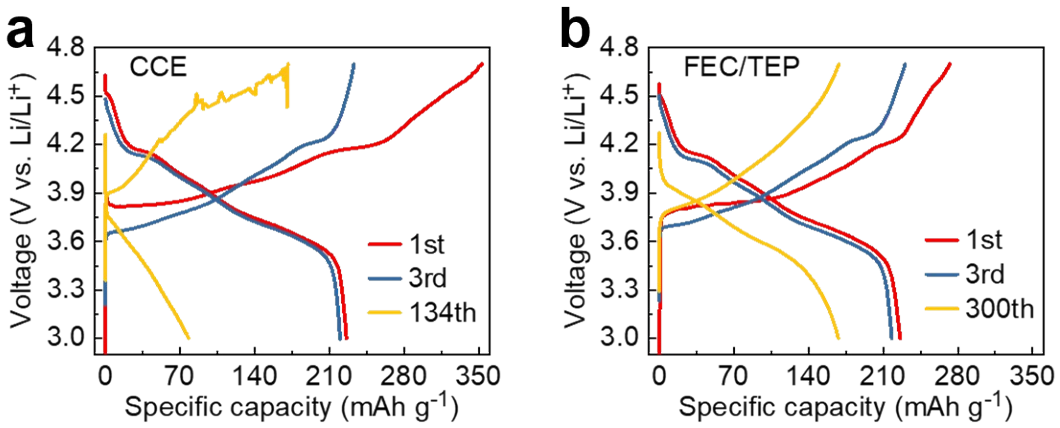

Figure S22. Charge-discharge curves of Li||NCM811 battery using CCE and the FEC/TEP electrolyte in the voltage range of 3-4.7 V.

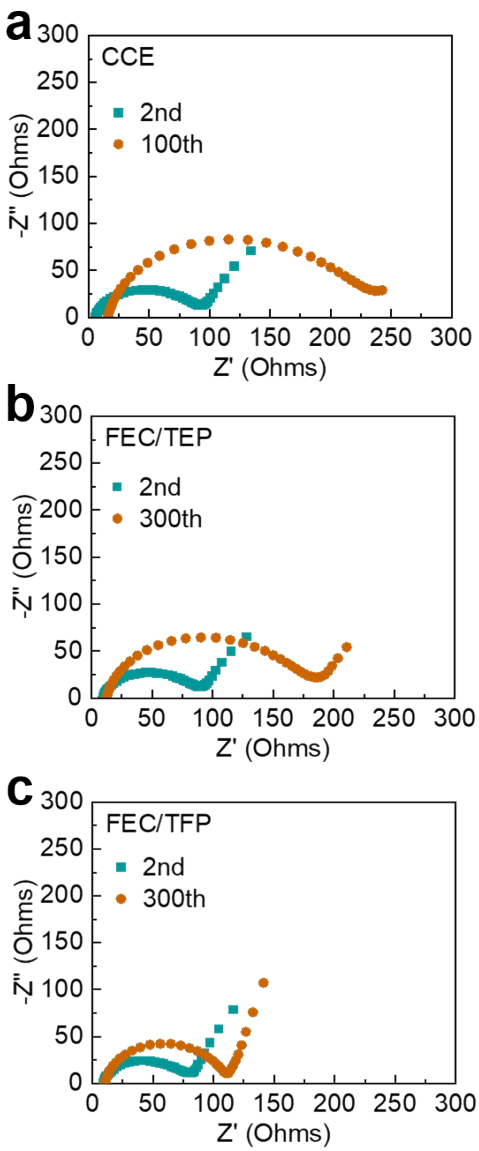

Figure S23. EIS tests of Li||NCM811 cells after cycling using (a) CCE and (b) the FEC/TEP and (c) FEC/TFP electrolyte, respectively.

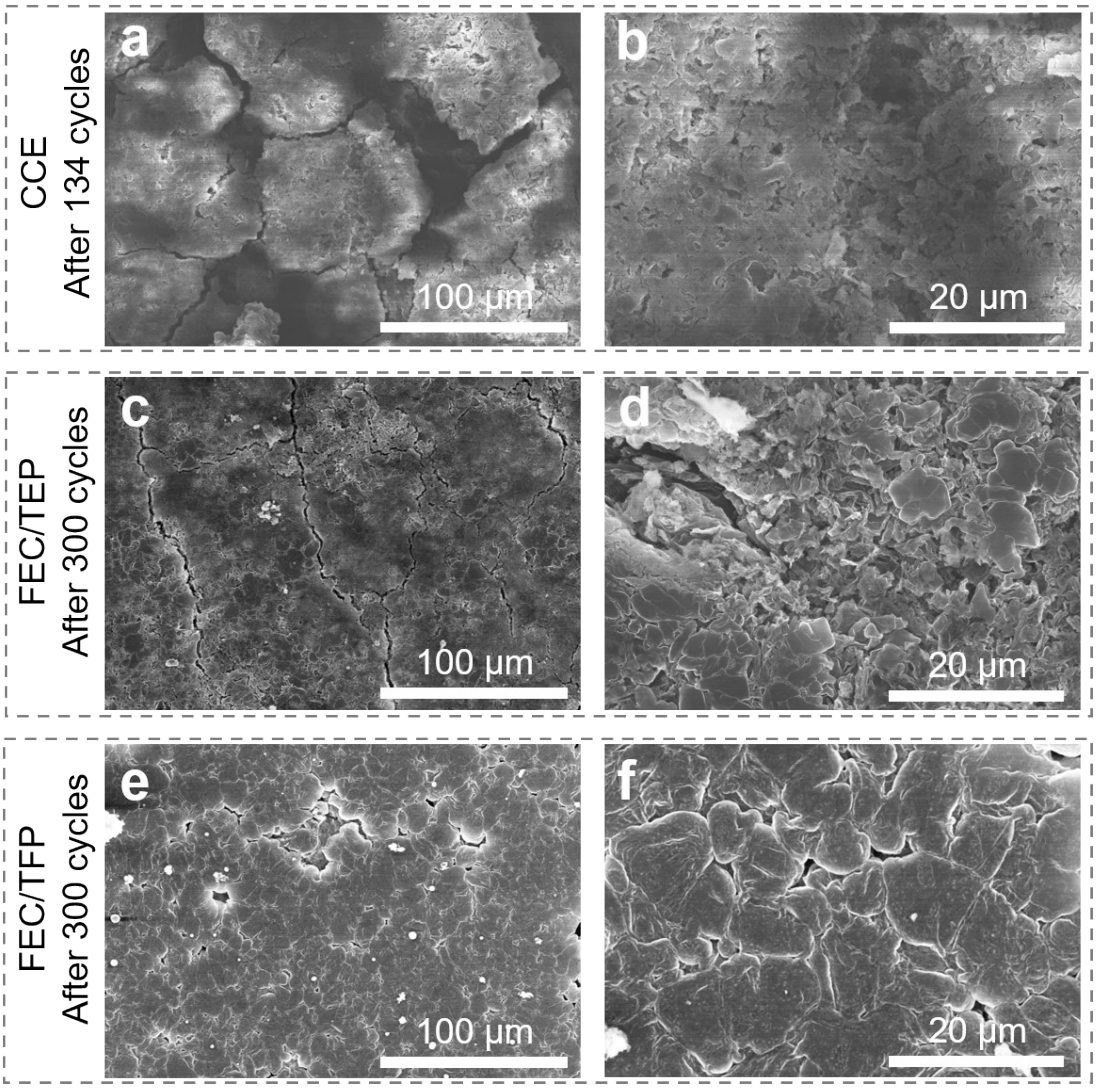

Figure S24. SEM images of lithium metal anode of Li||NCM811 battery after cycling with (a-b) CCE, (c-d) FEC/TEP and (e-f) FEC/TFP electrolyte, respectively.

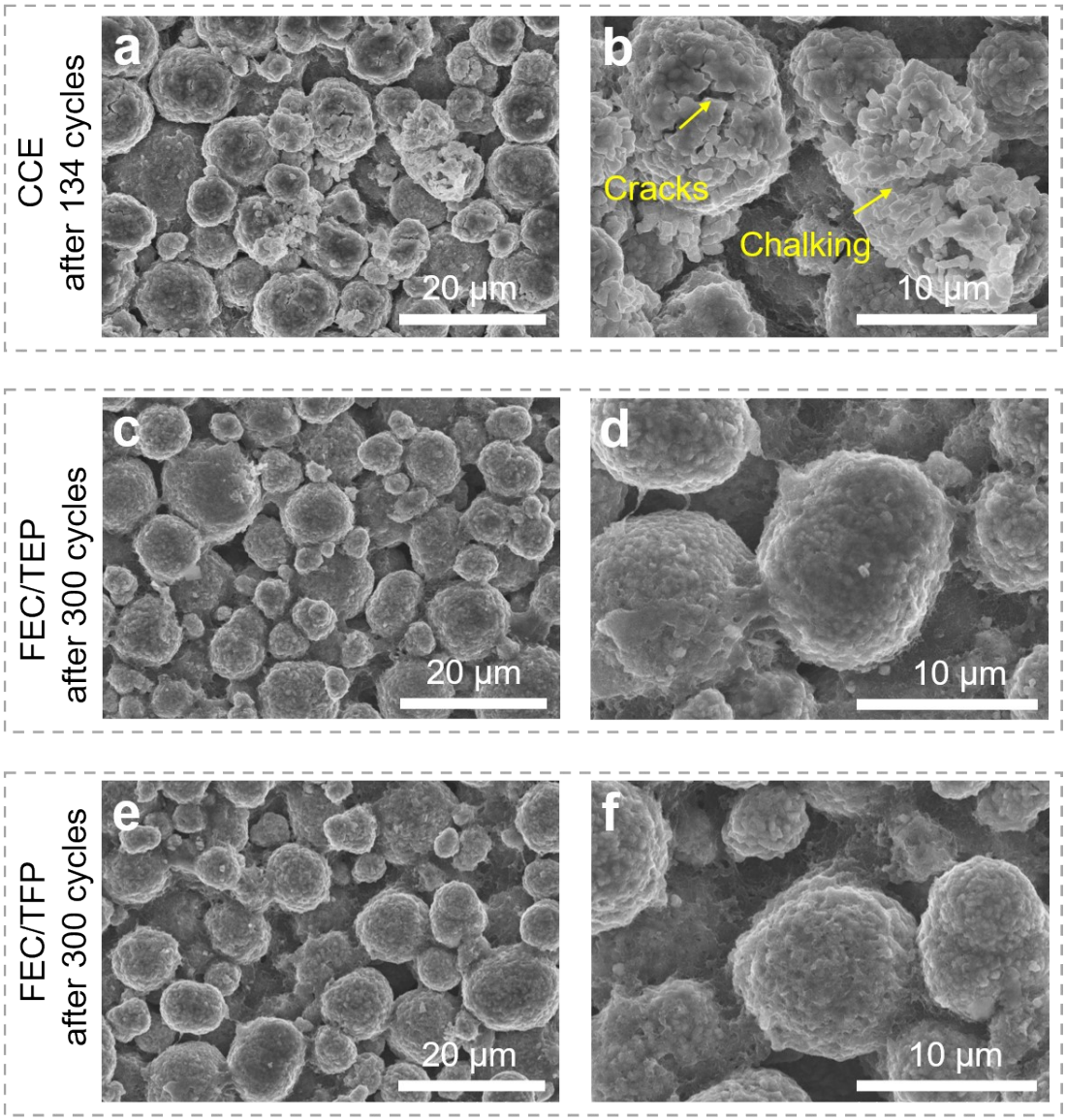

Figure S25. Top view SEM images of NCM811 cathode after cycling in Li||NCM811 cells with (a-b) CCE, (c-d) FEC/TEP and (e-f) FEC/TFP electrolyte, respecitivly.

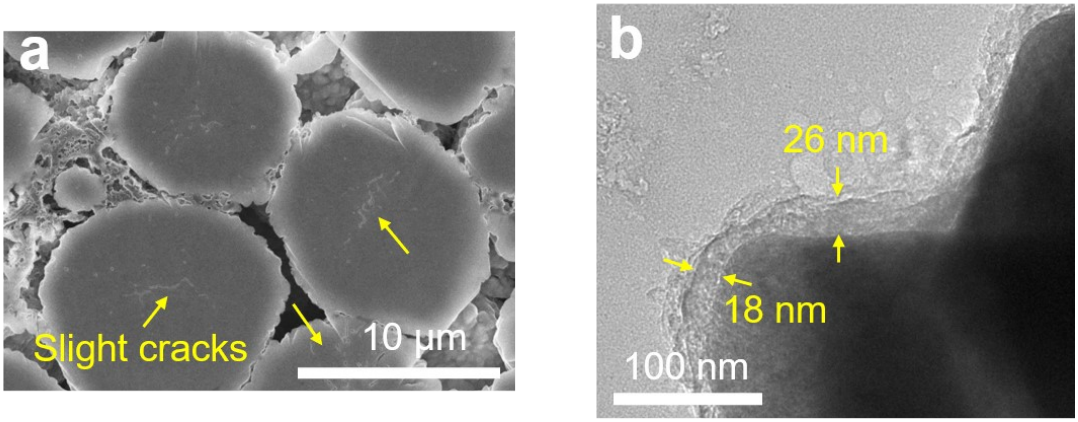

Figure S26. NCM811 cathode was observed after 300 cycles of Li||NCM811 cells using FEC/TEP electrolytes. (a) SEM image of NCM811 pacticles cross section. (b) TEM image of CEI on NCM811 pacticle surface.

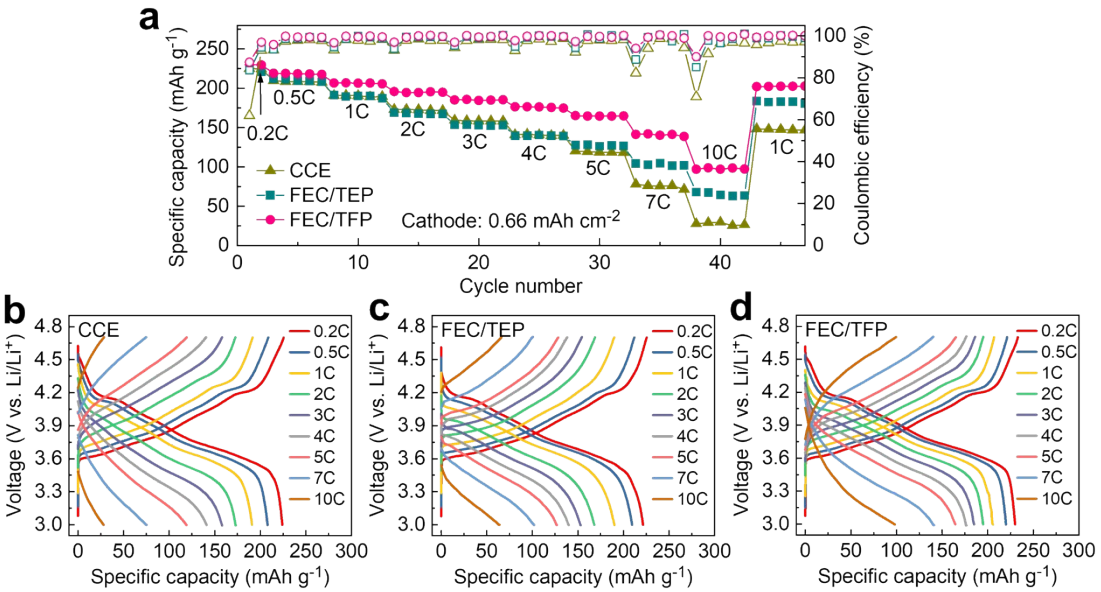

Figure S27. (a) C-rate test of Li||NCM811 battery in different electrolytes. Corresponding charge-discharge curves in (b) CCE (c) FEC/TEP and (d) FEC/TFP electrolyte.

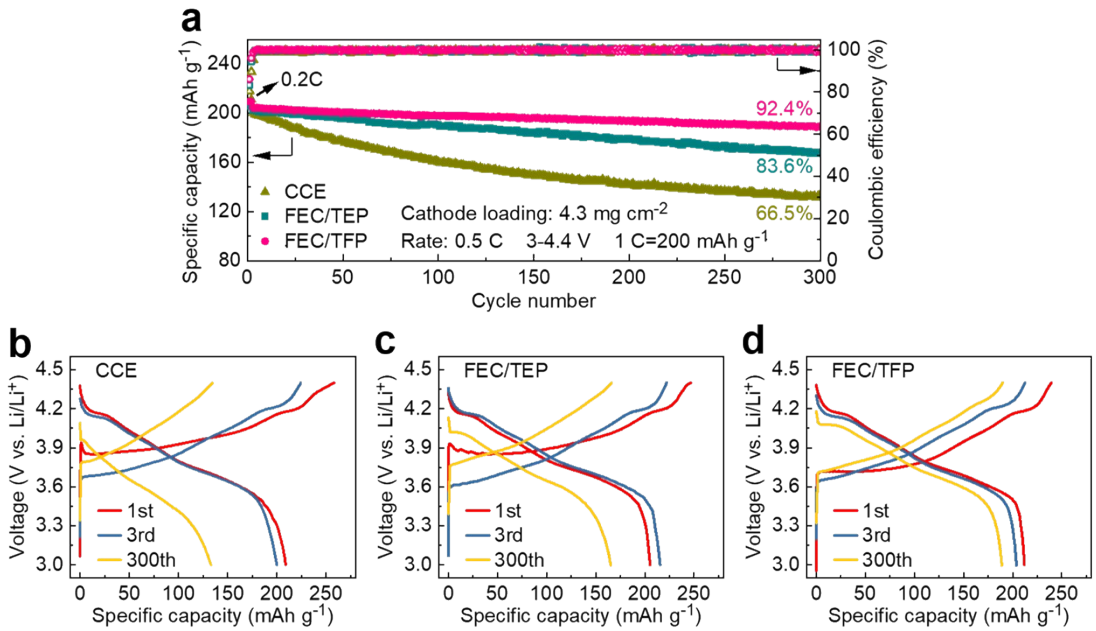

Figure S28. (a) Cycling performance measurements of Li||NCM811 battery with Li chips (1 mm thick) as anode at 3-4.4 V, and the corresponding charge-discharge curves in (b) CCE, (c) FEC/TEP and (d) FEC/TFP electrolyte.

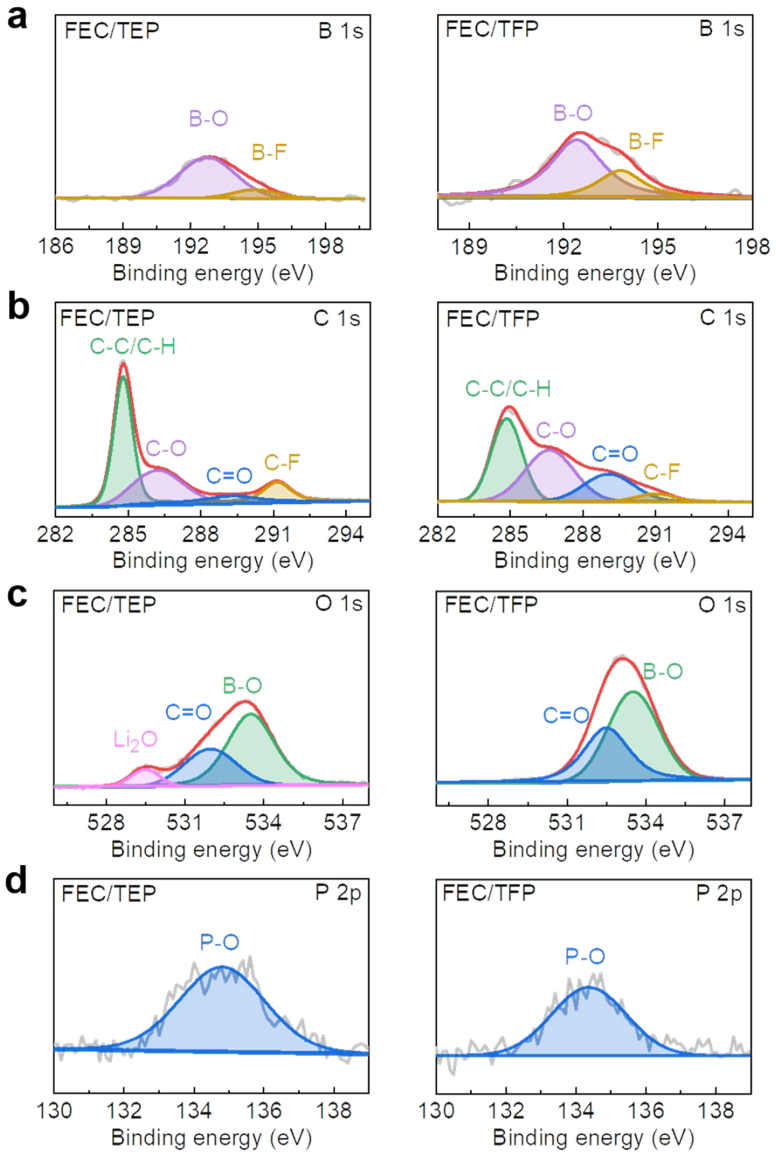

Figure S29. XPS spectra of NCM811 cathode CEI in different electrolytes.

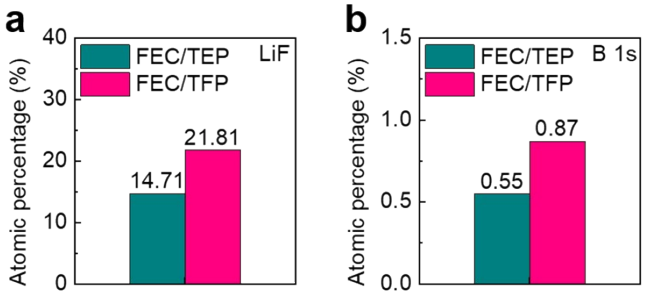

Figure S30. (a) LiF and (b) B atom content from XPS spectra of CEI formed on NCM811 cathode surface.

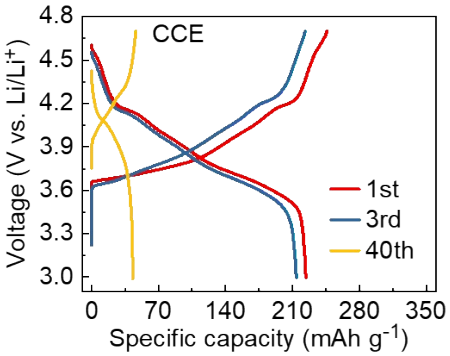

Figure S31. Charge-discharge curves of Li||NCM811 batteries under practical conditions.

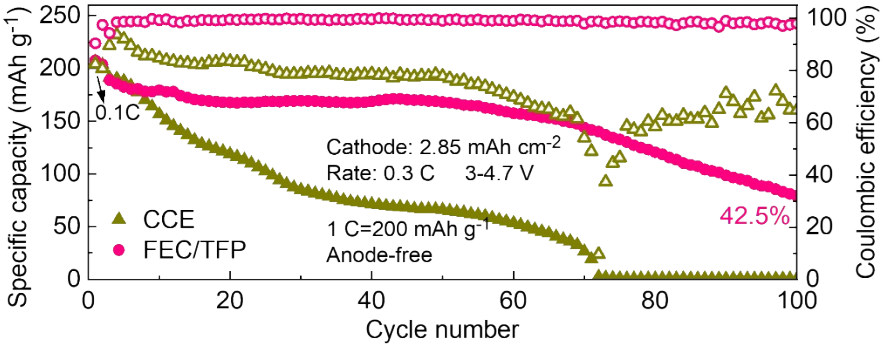

Figure S32. The cycling performance of anode-free lithium metal batteries using different electrolytes.

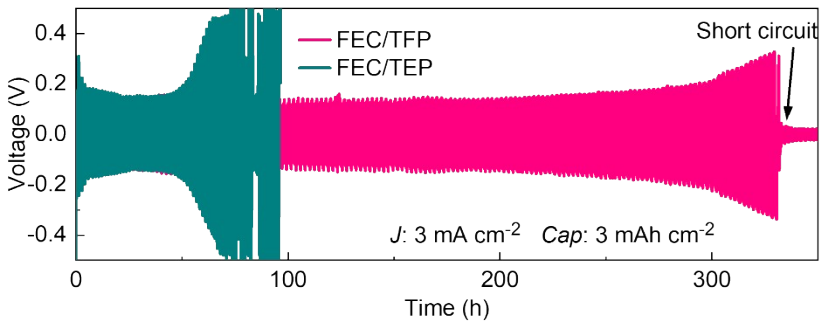

Figure S33. Long cycling test of Li//Li symmetric battery at 3 mA cm^{-2}-3 mAh cm^{-2}.

Table S2. Performance comparison of lithium metal full batteries.

Electrolyte	Cathode	Cut-off voltage	Electrolyte	N/P	Specific energy(wh kg^{-1})	Cycle number	Flammability	Literature
0.6 M $LiPF_6$+1.2 M $LiNO_3$ in EC/DEC/FEC/TMP	NCM811(4.75 mAh cm^{-2})	4.4	10 µL mAh^{-1}	5	629	100	Nonflammable	7
1 M $LiPF_6$ FEC/FEMC/HFE	NCM811 (2 mAh cm^{-2})	4.4	100 µL (flooded)	1	680	120	Nonflammable	8
0.8M Pyr14FSI+0.2M LiTFSI	NCM88 (1.9 mAh cm^{-2})	4.3	N/A	~5.3	564	300	Nonflammable	9
LiFSI:EmimFSI:dFBn 1:2:2 by mol	NCM811 (10 mg cm^{-2}	4.4	N/A	~1	733	250	Nonflammable	10
1M $LiBF_4$ +1M LiDFOB tFEP/FEC	NCM811 (4.64 mAh cm^{-2})	4.6	2.75 g Ah^{-1}	Anode-free	442.5	100	Flammable	11
1 M LiFSI/DMTMSA	NCM811 (4 mAh cm^{-2})	4.7	2.62 g Ah^{-1}	0.39	353	90	Flammable	12
1M $LiPF_6$ EMC/FEC+3$LiNO_3$+TPFPB	NCM811 (4.03 mAh cm^{-2})	4.5	3.4 g Ah^{-1}	2.3	295.1	140	Flammable	13
LiFSI-1.2DME-3TTE	NCM811 (4.2 mAh cm^{-2})	4.4	3 g Ah^{-1}	2.38	325	160	Flammable	4
2M LiFSI BFE	NCM811(3.5 mAh cm^{-2})	4.4	2.4 g Ah^{-1}	2.8	426	200	Flammable	14
FEC/TFP	NCM811 (4.78 mAh cm^{-2})	4.7	5 µL mAh^{-1}	2	692	120	Nonflammable	This work

Reference

1 X. Fan, L. Chen, X. Ji, T. Deng, S. Hou, J. Chen, J. Zheng, F. Wang, J. Jiang, K. Xu and C. Wang, *Chem*, 2018, **4**, 174-185.

2 S. Jiao, X. Ren, R. Cao, M. H. Engelhard, Y. Liu, D. Hu, D. Mei, J. Zheng, W. Zhao, Q. Li, N. Liu, B. D. Adams, C. Ma, J. Liu, J.-G. Zhang and W. Xu, *Nat. Energy*, 2018, **3**, 739-746.

3 Q.-K. Zhang, X.-Q. Zhang, L.-P. Hou, S.-Y. Sun, Y.-X. Zhan, J.-L. Liang, F.-S. Zhang, X.-N. Feng, B.-Q. Li and J.-Q. Huang, *Adv. Energy Mater.*, 2022, **12**, 2200139.

4 X. Ren, L. Zou, X. Cao, M. H. Engelhard, W. Liu, S. D. Burton, H. Lee, C. Niu, B. E. Matthews, Z. Zhu, C. Wang, B. W. Arey, J. Xiao, J. Liu, J.-G. Zhang and W. Xu, *Joule*, 2019, **3**, 1662-1676.

5 S. Jurng, Z. L. Brown, J. Kim and B. L. Lucht, *Energ. Environ. Sci.*, 2018, **11**, 2600-2608.

6 J. A. Weeks, J. N. Burrow, J. Diao, A. G. Paul-Orecchio, H. Srinivasan, R. R. Vaidyula, A. Dolocan, G. Henkelman and C. B. Mullins, *Adv. Mater.*, 2023, **n/a**, 2305645.

7 Z. Wang, Y. Wang, B. Li, J. C. Bouwer, K. Davey, J. Lu and Z. Guo, *Angew. Chem. Int. Ed.*, 2022, **61**, e202206682.

8 X. Fan, L. Chen, O. Borodin, X. Ji, J. Chen, S. Hou, T. Deng, J. Zheng, C. Yang, S.-C. Liou, K. Amine, K. Xu and C. Wang, *Nat. Nanotechnol.*, 2018, **13**, 715-+.

9 F. Wu, S. Fang, M. Kuenzel, A. Mullaliu, J.-K. Kim, X. Gao, T. Diemant, G.-T. Kim and S. Passerini, *Joule*, 2021, **5**, 2177-2194.

10 X. Liu, A. Mariani, T. Diemant, M. E. D. Pietro, X. Dong, M. Kuenzel, A. Mele and S. Passerini, *Adv. Energy Mater.*, 2022, **12**, 2200862.

11 M. Mao, X. Ji, Q. Wang, Z. Lin, M. Li, T. Liu, C. Wang, Y.-S. Hu, H. Li, X. Huang, L. Chen and L. Suo, *Nat. Commun.*, 2023, **14**, 1082.

12 W. Xue, M. Huang, Y. Li, Y. G. Zhu, R. Gao, X. Xiao, W. Zhang, S. Li, G. Xu, Y. Yu, P. Li, J. Lopez, D. Yu, Y. Dong, W. Fan, Z. Shi, R. Xiong, C.-J. Sun, I. Hwang,

W.-K. Lee, Y. Shao-Horn, J. A. Johnson and J. Li, *Nat. Energy*, 2021, **6**, 495-505.

13 S. Li, W. Zhang, Q. Wu, L. Fan, X. Wang, X. Wang, Z. Shen, Y. He and Y. Lu, *Angew. Chem. Int. Ed.*, 2020, **59**, 14935-14941.

14 G. Zhang, J. Chang, L. Wang, J. Li, C. Wang, R. Wang, G. Shi, K. Yu, W. Huang, H. Zheng, T. Wu, Y. Deng and J. Lu, *Nat. Commun.*, 2023, **14**, 1081.